



# **JGR** Atmospheres

### RESEARCH ARTICLE

10.1029/2025JD043922

### **Key Points:**

- A multiple parallel rainband (MPRB) in the Beibu Gulf formed via backbuilding over HCRs elevated by mountains
- Mountains from 200 m in valleys to 600 m at peaks are favorable for the MPRB formation through accumulating water vapor and lifting HCRs
- Mountains that are too high or too low are not favorable for the MPRB formation because of HCRs being destroyed or inadequately elevated

#### Correspondence to:

Z. Meng, zymeng@pku.edu.cn

#### Citation:

Wang, P., & Meng, Z. (2025). Influences of horizontal convective rolls and complex terrain on the structure of mesoscale convective systems with multiple parallel rainbands. *Journal of Geophysical Research: Atmospheres, 130*, e2025JD043922. https://doi.org/10.1029/2025JD043922

Received 22 MAR 2025 Accepted 11 SEP 2025

## Influences of Horizontal Convective Rolls and Complex Terrain on the Structure of Mesoscale Convective Systems With Multiple Parallel Rainbands

Peiyu Wang<sup>1</sup> and Zhiyong Meng<sup>1</sup>



<sup>1</sup>Department of Atmospheric and Oceanic Sciences, School of Physics, and China Meteorological Administration Tornado Key Laboratory, Peking University, Beijing, China

**Abstract** This study investigates the formation mechanism of the multiple parallel rainbands' (MPRB) organizational mode in a mesoscale convective system (MCS) that occurred on 12 August 2017, in the Beibu Gulf—a region with the highest frequency of MPRBs in China. The analysis is conducted using the Weather Research and Forecasting (WRF) model through 1-km high-resolution simulation and terrain modification experiments. The results indicated that the MPRB formed through backbuilding processes, primarily over horizontal convective rolls (HCRs), elevated by low mountains along the coastline. The results showed that mountains from 200 m in valleys to 600 m at peaks did not disrupt HCR formation. Instead, mountains of these heights helped elevate HCRs, thereby facilitating convection initiation. However, after increasing the mountain heights above valley heights by 50%, the higher terrain and larger distance between valleys and peaks decreased boundary layer wind and 0–1 km vertical wind shear, preventing HCR formation and thereby suppressing the development of the MPRB. In contrast, lowering the terrain height reduced the HCR height, thereby weakening or even eliminating MPRB even though it enhanced the organization of HCRs. HCR formation in this case was attributed to convective instability with high vertical wind shear and rich moisture. Coastal mountains functioned as barriers, blocking the flow of moisture from the southern sea, which was also essential for HCR formation and convection initiation.

Plain Language Summary Multiple parallel rainbands (MPRBs) constitute a series of parallel rainbands that are often associated with heavy rainfall. In this study, the formation mechanism of one MPRB case in the Beibu Gulf, which is the region with the highest frequency of MPRBs in China, was investigated. Horizontal convective rolls (HCRs), which are counter-rotating horizontal vortices that commonly occur within the convective boundary layer, are frequently observed in this region, but no studies have linked their formation to MPRBs. The results indicated that MPRB formed via new thunderstorm cells repeatedly forming upwind of existing storms along the updraft branches of HCRs elevated by low mountains. Notably, the structure of HCRs and the evolution of MPRB were highly sensitive to the height of the mountains.

### 1. Introduction

Mesoscale convective systems (MCSs) exhibit diverse organizational modes with various juxtapositions of convective and stratiform rainfall regions (Li et al., 2021; Parker & Johnson, 2000; Zheng et al., 2013). Different types of organizations can cause varying types of severe weather. Gallus et al. (2008) classified convective storms into nine primary organizational patterns and found that leading-stratiform and parallel stratiform systems are most prone to producing hail and tornadoes, bow echoes are associated with the most severe straight-line winds, and trailing-stratiform systems have the highest propensity for generating flooding.

Luo et al. (2014) found a special organizational mode of MCSs, multiple parallel rainbands (MPRBs), during an event that caused extreme precipitation in East China. The extreme precipitation was primarily attributed to the presence of two different scales of train effect (Luo et al., 2014). Train effect refers to an organizational pattern where convective cells are aligned in a linear fashion and repeatedly pass over the same area, much like a train (Doswell et al., 1996). Since precipitation amount is generally proportional to both the precipitation rate and its duration, train effect tends to produce heavy precipitation. Since almost all MPRBs are accompanied by at least one type of train effect, they commonly result in heavier precipitation than that induced by ordinary MCSs (Wang & Meng, 2023). For example, an MPRB event on 10 May 2013, yielded 298 mm of accumulated rainfall in East China (Luo et al., 2014), and two additional MPRB cases on 10 May 2013, and 11 May 2014, produced extreme

© 2025. American Geophysical Union. All Rights Reserved.

WANG AND MENG 1 of 18

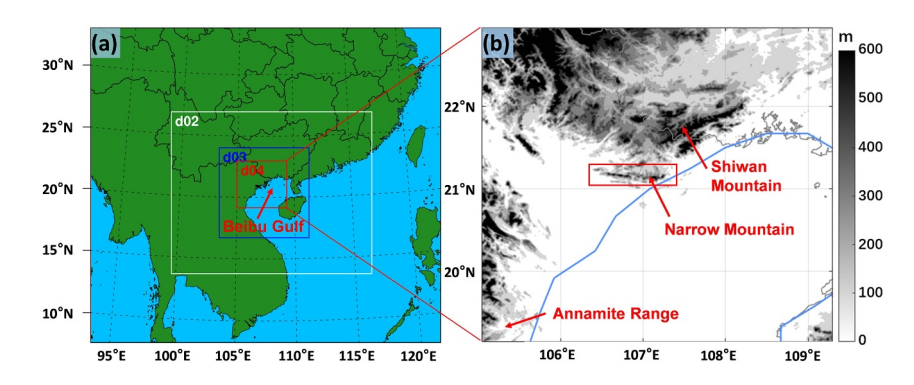


**Figure 1.** (a) WRF simulation domains and (b) terrain height of simulation domain d04 (shading; m); the red rectangle denotes the location of the narrow mountain along the western coast of the Beibu Gulf. The blue line denotes the coastline in a coarse resolution.

rainfall of 451 mm in coastal south China (Liu et al., 2018; Wang et al., 2014). This work aims to examine the formation mechanism of an MPRB under complex terrain conditions.

As a specific organizational mode of MCSs, the formation mechanism of MPRBs remains poorly understood, particularly under complex terrain conditions. Wang and Meng (2023) proposed the criteria for identifying MPRBs as follows: (a) At least three rainbands must simultaneously exist for more than 20 min; (b) the angles between the major axes of all rainbands must be less than 45° to ensure that the rainbands are approximately parallel to each other; and (c) along the entire major axis of any rainband within the examined MPRB system, there must be at least one point where a straight line drawn parallel to its minor axis intersects another rainband, ensuring that the rainbands are not too far apart in the direction along the major axis of the parent MPRB. Wang and Meng (2023) defined two types of MPRBs according to their formation processes, namely, initiation-and differentiation-type MPRBs. Initiation-type MPRBs occur at the initiation stage of their parent MCSs, when most rainbands initiate and develop individually. Differentiation-type MPRBs mainly form through the splitting of long rainbands.

For differentiation-type MPRBs, Liu et al. (2018) reported that system-relative rear inflows led to rainband splitting and reestablishment and thus facilitated the formation of MPRBs. In contrast, the formation mechanisms of initiation-type MPRBs have been attributed primarily to outflows of cold pools in the literature. Wang et al. (2014) emphasized that the lifting of warm air by cold outflows created echo training and MPRB. Wang et al. (2021) further proposed a two-stage formation process for the MPRB in their case study: the first stage was initiated by cold pool outflows, while the second stage was forced by lifting of outflows by parallel mountain valleys. These formation mechanisms only interpret those initiation-type MPRBs that form following a preceding MCS from which cold pool develops. However, the formation mechanism of those initiation-type MPRBs without a preceding MCS have not been explored.

The highest occurrence frequency of MPRBs in China is located in the northern Beibu Gulf and its coastal areas, with minor high-frequency occurrences in Guangdong, northern Jiangxi, and southern Shandong provinces. The region with the highest frequency of initiation-type MPRBs occurs in the mountainous areas in the north of the Beibu Gulf (Figure 1a). This study aims to investigate the formation mechanism of an initiation-type MPRB case without preceding MCS in the Beibu Gulf in China on the basis of numerical simulations. This kind of initiation-type MPRBs accounts for about 64% of all initiation-type MPRBs in the northern Beibu Gulf and its coastal areas.

The Beibu Gulf is surrounded on three sides by land (Figure 1a) and exhibits complex terrain along the western coastline (Figure 1b). To the north of the western coast lies Shiwan Mountain and its branches, with elevations ranging from 200 to 1,000 m above sea level (ASL). The ground level in this area is 10 m ASL. On the southern side, near the coastline, a narrow mountain range peaks at 700 m ASL with an average peak of 600 m, with valleys approximately 200 m ASL high. Statistics show that more than half of the MPRBs in the northern Beibu Gulf occurred over this complex terrain along the western coast (Wang & Meng, 2023).

The complex terrain surrounding the Beibu Gulf possibly contributes to the occurrence of intricate planetary boundary layer (PBL) features. According to Zhang and Meng (2019) and Du et al. (2022), the Beibu Gulf serves as a high-frequency center of southwesterly boundary layer low-level jets (BLLJs), facilitating strong boundary

WANG AND MENG 2 of 18

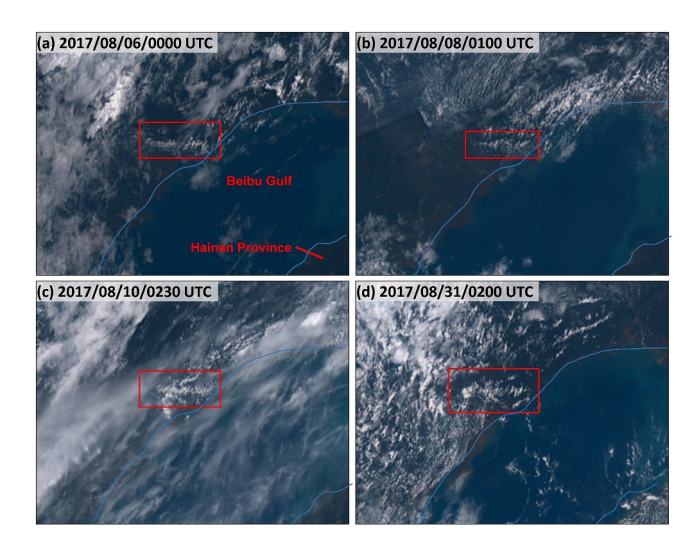


**Figure 2.** Snapshots of satellite images obtained at (a) 0000 UTC on 06 August 2017, (b) 0100 UTC on 08 August 2017, (c) 0230 UTC on 10 August 2017, and (d) at 0200 UTC on 31 August 2017 retrieved from the Himawari-8 satellite website at https://himawari8.nict.go.jp/. The red rectangle denotes the location of HCRs. The light blue line denotes the coastal line in a coarse resolution

layer vertical wind shear. Kong et al. (2020) reported that BLLJs are driven mainly by upstream, continental, and nocturnal LLJs crossing over the Annamite Range of Vietnam (Figure 1b). Owing to the high vertical shear associated with BLLJs, horizontal convective rolls (HCRs) are frequently observed near the western coastal area of the Beibu Gulf. For example, seven HCR events were observed in August 2017, as shown in images captured in the visible channel of the Himawari-8 satellite (selected cases are shown in Figure 2).

HCRs are counter-rotating horizontal vortices commonly observed within the convective boundary layer (American Meteorological Society, 2024). Their major axes are aligned with the mean boundary layer wind-shear vector, and the depth of roll circulations corresponds to the boundary layer depth. HCRs generally persist for 1–6 hr with aspect ratios between 1 and 7 (Banghoff et al., 2020), defined as the ratio of wavelength in terms of the spacing between updraft regions along the cross-roll direction, which is generally 2–10 km (Young et al., 2002), to boundary layer depth. Under certain water vapor and energy conditions, convergent lifting above updraft branches can produce cloud streets (Su et al., 2022). Thermal instability, inflection point instability, and parallel instability are considered the primary causes of HCRs (Etling & Brown, 1993). Previous studies have shown that HCRs alone rarely initiate deep convection due to their weak lifting, but when they intersect with other boundaries such as drylines (Xue & Martin, 2006), gust fronts, or sea-

breeze fronts (Fovell, 2005; Zhu et al., 2021), the resulting triple points with strong convergence and lifting may promote deep convective development. Given the parallel cloud structure and the frequent occurrence of HCRs in the Beibu Gulf with complex terrain, it is extremely important to explore whether the combination of HCRs with complex terrain facilitates the formation of MPRBs in this area.

This study aimed to elucidate the formation mechanism of an initiation-type MPRB over the Beibu Gulf at 2142 Coordinated Universal Time (UTC) on 12 August (4:42 local standard time (LST) on 13 August), 2017. The data and methods are outlined in Section 2, followed by an overview of the MPRB case in Section 3. Section 4 presents the simulation results and an analysis of the MPRB formation mechanism. The main conclusions and discussion are provided in Section 5.

### 2. Data and Methods

A regional radar mosaic of basic reflectivity provided by the China Meteorological Administration was employed to track the initiation and evolution of MCSs and the formation of MPRB. The radar mosaic is generated by selecting the optimal reflectivity value from the three lowest elevation angles (i.e.,  $0.5^{\circ}$ ,  $1.5^{\circ}$ , and  $2.4^{\circ}$ ) at each location (Bai et al., 2020), commonly referred to as a terrain-based hybrid scan (Fulton et al., 1998). In addition, fifth-generation reanalysis (ERA5) data from the European Center for Medium-Range Weather Forecasts (ECMWF) with a horizontal resolution of  $0.25^{\circ} \times 0.25^{\circ}$  were used to analyze environmental parameters (Hersbach et al., 2023a, Hersbach et al., 2023b).

The Weather Research and Forecasting (WRF) model version 4.4 was used to simulate the selected case, employing four horizontal domains with grid spacings of 27, 9, 3, and 1 km (Figure 1). The initial and lateral boundary conditions were provided by final operational global analysis (FNL; National Centers for Environmental Prediction/National Weather Service/NOAA/U.S. Department of Commerce 2000) data gridded at  $1^{\circ} \times 1^{\circ}$  with 6-hr intervals. Domain 1 was initiated at 0600 UTC (1400 LST) on 12 August 2017, and the other three domains were initiated at 1200 UTC (2000 LST) on 12 August 2017. All the domains were integrated to 0600 UTC on 13 August 2017.

In all four simulation domains, the Morrison double-moment microphysics scheme (Morrison et al., 2009), the CAM longwave and shortwave schemes (Collins et al., 2004), the Yonsei University PBL scheme (Hong et al., 2006), the revised MM5 surface layer scheme (Jimenez et al., 2012), and the 5-layer thermal diffusion land surface model (Dudhia, 1996) were adopted. The Grell-Freitas (GF) cumulus parameterization scheme (Grell & Freitas, 2014) was applied in domains 1 and 2 only.

WANG AND MENG 3 of 18

Table 1           Configurations of Terrain Sensitivity Experiments	
Name	Terrain modification in the area denoted respectively in Figure 3
MTs400	Terrain exceeding 400 m ASL was reduced to 400 m ASL
MTs200	Terrain exceeding 200 m ASL was reduced to 200 m ASL
MTs20	Terrain exceeding 20 m ASL was reduced to 20 m ASL
MTsAdd	Terrain exceeding 200 m ASL was added to 150% of its original height
MTsSmall	Terrain of the narrow mountain exceeding 20 m ASL was reduced to 20 m ASL
MTsBig	Terrain of the Shiwan Mountain exceeding 20 m ASL was reduced to 20 m ASL

Given that the MPRB event occurred in the coastal narrow mountain range region (denoted as "Narrow Mountain" in Figure 1b) immediately south of Shiwan Mountain, we hypothesized that the formation of MPRB may have been influenced by both Shiwan Mountain and the narrow mountain. To explore the impact of these mountains on the evolution of the target MPRB system, in addition to the control (CNTL) experiment, six sensitivity experiments were designed by adjusting the height of mountain ranges in all four domains (Table 1, Figure 3).

Instead of using the strict square area for terrain modification (denoted in Figure 3), we manually selected the boundary of the Shiwan Mountain in the north and northwest boundaries of the square region to avoid a truncation shock in terrain height. Considering that the mountain peaks in the Beibu Gulf are approximately 600 m ASL and the valleys are around 200 m ASL, we selected 400 m ASL and 200 m ASL as the thresholds for a gradual terrain modification. MTs400 was designed to reduce the terrain exceeding 400 m ASL to 400 m ASL in the area denoted by the maroon square (Figure 3a), in which the vertical distance between peaks and valleys was decreased approximately by half. MTs200 was the same as MTs400 but the height of mountains exceeding 200 m ASL was reduced to 200 m ASL (Figure 3b), in which the mountain peaks were generally removed. In the MTs20 experiment, the height of mountains higher than 20 m ASL was reduced to 20 m ASL (Figure 3c), with the goal of removing both mountains. In the MTsAdd experiment, the height of mountains higher than 200 m ASL was increased to 150% of its original height (Figure 3d); thereby, not only the height of mountains but also the vertical distance between peaks and valleys were increased. In the MTsSmall experiment, the narrow mountain was removed by reducing the terrain above 20 m ASL in the maroon square in Figure 3e to 20 m ASL. In contrast, in the MTsBig experiment, only the narrow mountain was retained, while the terrain height above 20 m ASL in the Shiwan Mountain area (denoted by the maroon square in Figure 3f) was reduced to 20 m ASL. Additionally, the RH90 experiment was conducted to explore the impact of the relative humidity on the formation of MPRB. In this experiment, the relative humidity below 2 km ASL across the entire area of domain 1 was decreased by 10% of its original values in the control experiment at the initial time.

### 3. Case Overview

The MPRB system was initiated in the narrow mountain range during the early morning on 12 August 2017. Radar mosaics show that two convective cells formed in the narrow mountain at 1954 UTC (Figure 4a). A new convective cell was subsequently initiated on the eastern side of the previous cells 18 min later (Figure 4b). These three cells independently evolved into three distinct short rainbands oriented along the southwest-northeast direction by 2142 UTC (Figure 4c) and formed an MPRB system.

With the formation of the MPRB system at 2142 UTC, a fourth convective cell emerged to the northeast of the three rainbands (Figure 4c). In addition, all four rainbands essentially remained quasi-stationary. The MPRB structure lasted more than one and a half hours. During this period, all the rainbands developed individually, rather than through splitting of long rainbands. Wang and Meng (2023) defined this event as an initiation-type MPRB system. Subsequently, rainband 4 shifted to the northeast, while the other three rainbands weakened, thereby transitioning to stratiform precipitation. By 0200 UTC on 13 August, the entire MPRB system had dissipated.

WANG AND MENG 4 of 18

21698996, 2025, 18, Downloaded from https://agupubs.onlinelibrary.wiley.com/doi/10.1029/2025JD043922 by Peking University Health, Wiley Online Library on [25/09/2025]. See the Terms and Conditions (https://onlinelibrary.wiley

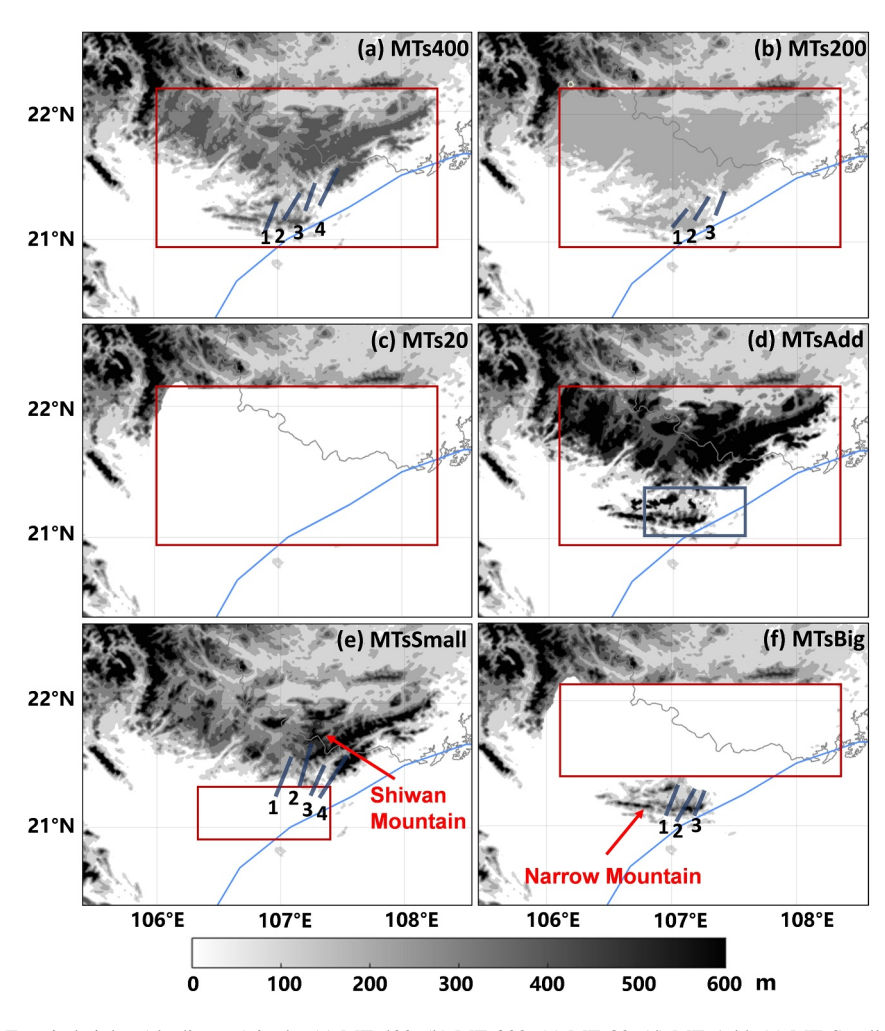


**Figure 3.** Terrain heights (shading; m) in the (a) MTs400, (b) MTs200, (c) MTs20, (d) MTsAdd, (e) MTsSmall, and (f) MTsBig experiments. The heavy blue lines denote their respective MPRB when they started to have the largest number of rainbands. The light blue line denotes the coastal line in a coarse resolution. The region for terrain modification is denoted by a maroon square in each experiment. The blue box in (d) denotes where the MCS was located at peak intensity time in MTsBig.

ERA5 reanalysis data showed that this MPRB process occurred within a southwesterly flow to the west of the subtropical high and in front of a westerly trough at 500 hPa (Figure 5a). Warm, moist southerly flow from the ocean provided abundant moisture in the lower troposphere (Figure 5b). This MPRB system was located at the exit of a 925-hPa jet and the entrance of an 850-hPa jet (Figures 5c and 5d). This wind field is consistent with one type of coastal marine boundary layer jet event that occurs over the Beibu Gulf (BLJ\_WEST) (Du et al., 2022). The juxtaposition of the 925-and 850-hPa jets resulted in convergence at 925 hPa and divergence at 850 hPa near the coastal area, promoting substantial dynamic lifting and facilitating convection initiation (Du & Chen, 2019). Similar convergence at 925 hPa and divergence at 850 hPa were observed in the jet area in this case (Figures 5e and 5f, respectively).

### 4. Results

### 4.1. Control Experiment

The CNTL experiment adequately captured the evolution of the MPRB system (Figure 6). Two cells initiated simultaneously, with their timing and locations closely matching the observations, showing only an ~20-min time lag. By 2100 UTC, the simulated MCS met the criteria of MPRBs (Figure 6c). Moreover, the MPRB structure persisted until 2230 UTC (Figure 6e). Finally, the MCS dissipated at 0200 UTC on 13 August, which agreed well

WANG AND MENG 5 of 18

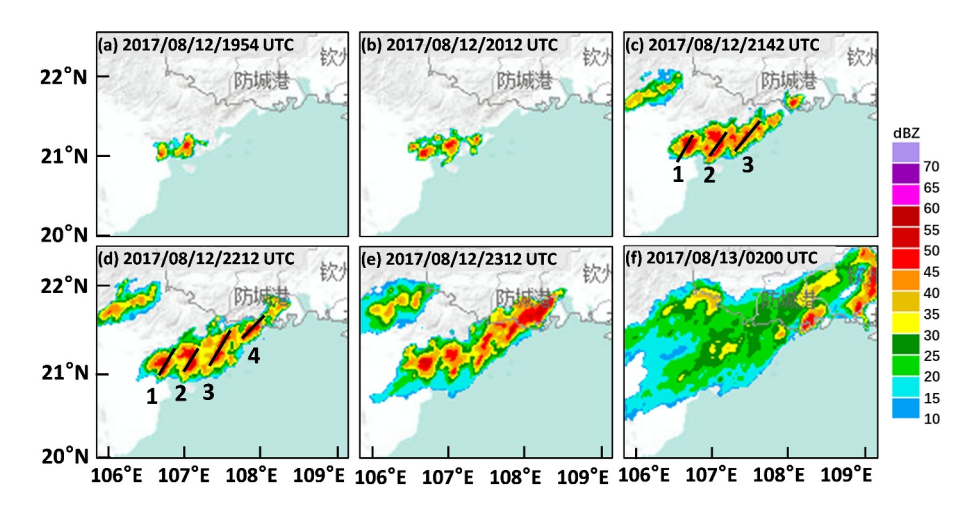


**Figure 4.** Mosaics of the composite radar reflectivity (shading; dBZ) for the MPRB case at (a) 1954 UTC, (b) 2012 UTC, (c) 2142 UTC, (d) 2212 UTC, (e) 2312 UTC on 12 August 2017, and (f) 0200 UTC on 13 August 2017. The black lines in (c) and (d) denote the rainbands of the MPRB system.

with the observed timeline. Even though the simulation generated two more rainbands than the observations, the simulation suitably facilitated the examination of the formation mechanism of this MPRB system.

To examine the formation mechanism of the MPRB system, the divergence field at 1 km ASL was analyzed. Clear alternating positive and negative divergence lines were observed at convection initiation time at 1950 UTC (Figure 7a). They occurred over the narrow mountain, oriented approximately along the north-south direction, parallel to the direction of low-level vertical wind shear with magnitude more than 10 m s<sup>-1</sup>. These alternating positive and negative convergence lines extended vertically to an altitude of approximately 2 km ASL (Figure 8a). The convergence/divergence below 1 km ASL generally corresponded to divergence/convergence above, coinciding with upward/downward motion, demonstrating a roll structure, rather than gravity wave. The average value of the roll aspect ratio was 6.2 over the narrow mountain region (denoted by the black box in Figure 7a), falling within the range of 1–7 for HCR statistics reported by Banghoff et al. (2020). Furthermore, we calculated the horizontal wind speed averaged in the boundary layer over the narrow mountain region (denoted by the black box in Figure 7a) at 1850 UTC, which was 20 min before the formation of the roll structure. The mean wind in the boundary layer was 7.09 m s<sup>-1</sup>, which was conducive to the formation of the HCR according to the threshold of  $U_{\rm CRI} > 6 \,\mathrm{m \, s}^{-1}$  of Santellanes et al. (2021). All these features were consistent with the characteristics of HCRs, as observed in satellite observations from the west coast area of the Beibu Gulf (Figure 2). Therefore, the roll structure was HCR. In terms of environmental characteristics, the pseudoequivalent potential temperature decreased with increasing height in lower troposphere at 1850 UTC (Figure 7b), suggesting the convective instability in the boundary layer, which further ruled out gravity waves. Consequently, HCR formed in this case due to convective instability rather than inflection point instability (Etling & Brown, 1993; Zhu et al., 2015).

Although HCRs are more likely to occur over flat areas, such as over the sea (Banghoff et al., 2020), the presence of topographic elements approximately 300 m above ground level (AGL) may not disrupt the structure of HCRs (Tian et al., 2003). Our numerical simulations and observational evidences showed that HCRs can form over mountains from 200 m ASL in valleys to 600 m ASL at peaks (with a sea level of 10 m).

The results indicated that the MPRB system might have formed through lifting by HCRs. The evolution of the horizontal divergence field at 1.8 km ASL around convective initiation (Figure 9) revealed that convective cells were initiated along the updraft branches of HCRs over the narrow mountain area. These updraft branches corresponded to the near-surface convergence and divergence above it at ~1.8 km ASL. At 1946 UTC, updraft branches of the HCRs reached altitudes above 1.8 km ASL, as revealed by the divergence at that level. Ten minutes later, convective cells were initiated above these updraft HCR branches. Next, new cells were continuously initiated in the southern part of the HCRs over the mountain area. With old cells moving downstream and new cells continuously initiated upstream, the MPRB system formed through a backbuilding process (Figures 9c and 9d). Figure 10 shows one example of such a backbuilding process for rainband 2. This rainband was initiated at 2000 UTC. Each slanted line represents the northward movement of a convective cell over time at a speed of

WANG AND MENG 6 of 18

18, Downloaded from https://agupubs.onlinelibrary.wiley.com/doi/10.1029/2025/D043922 by Peking University Health, Wiley Online Library on [25/09/2025]. See the Terms and Conditions (https://onlinelibrary.wiley

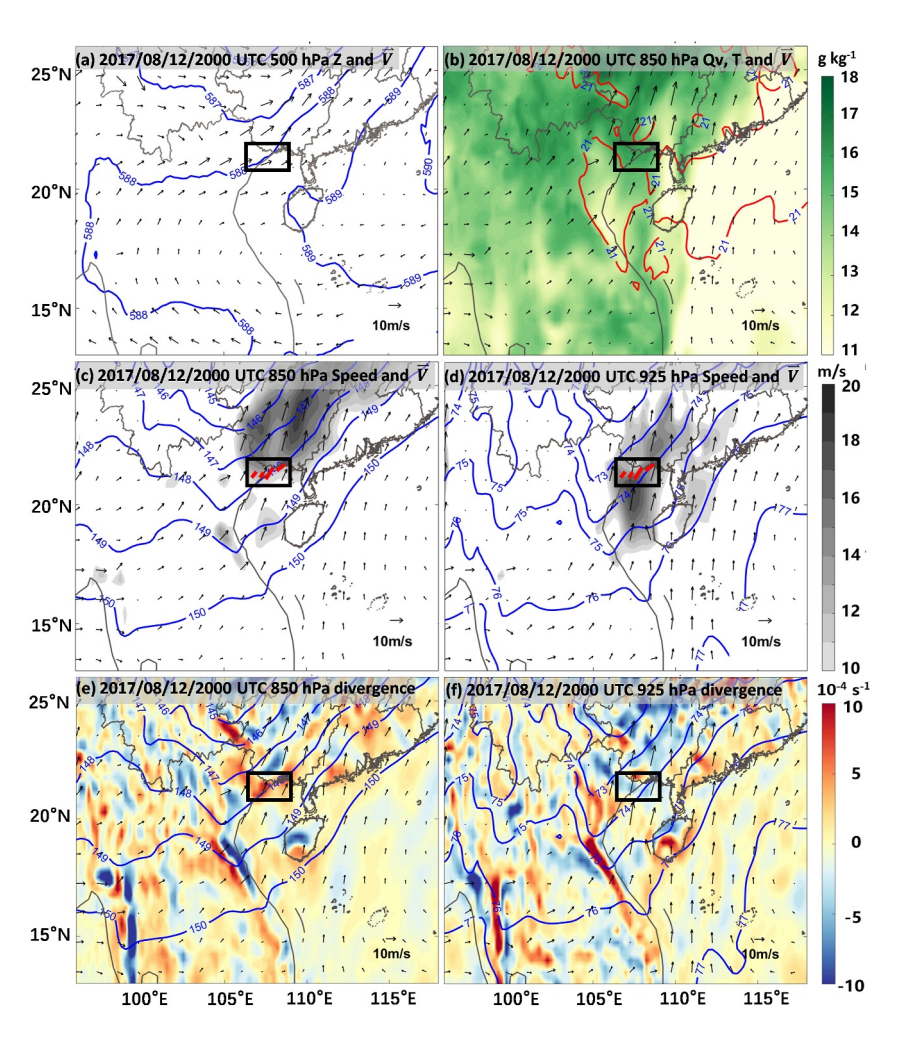


**Figure 5.** Synoptic environment of the case at 2000 UTC on 12 August 2017 revealed by ERA5 data analysis, including (a) the geopotential height (contoured in blue for every 10 gpm) and horizontal wind vector (black arrow; m s<sup>-1</sup>) at 500 hPa; (b) specific humidity (shading; g kg<sup>-1</sup>), temperature (contoured in red for 21°C), and horizontal wind vector (black arrow; m s<sup>-1</sup>) at 850 hPa; and (c) wind speed (shading; m s<sup>-1</sup>), geopotential height (contoured in blue for every 10 gpm), and horizontal wind vector (black arrow; m s<sup>-1</sup>) at 850 hPa. (d) is the same as (c) but for 925 hPa. (e) Divergence (shading;  $10^{-4}$  s<sup>-1</sup>), geopotential height (contoured in blue for every 10 gpm), and horizontal wind vector (black arrow; m s<sup>-1</sup>) at 850 hPa. (f) is the same as (e) but for 925 hPa. The red solid lines in (c) and (d) indicate the rainbands of the MPRB system. The location of the MPRB system is also denoted by a black box in all panels.

approximately  $8 \text{ m s}^{-1}$ . New convective cells continuously initiated near  $21.05^{\circ}\text{N}$  and propagated northward as time progressed, indicating the process of backbuilding. The entire backbuilding process lasted until 2200 UTC.

### 4.2. Sensitivity Experiments

### 4.2.1. Impact of the Coupling Between HCRs and Mountains on MPRB

The results of the sensitivity experiments revealed that the morphology and height of both Shiwan Mountain and the narrow mountain substantially influenced the formation time, location, intensity, and organization of the MPRB

In the MTs400 experiment (Figure 11a), in which peaks were lowered and the vertical distances between peaks and valleys were halved, MPRB was observed but less organized than that in the CNTL experiment. Only three rainbands were generated at 2120 UTC. In the MTs200 experiment (Figure 11b), in which all the mountain peaks were removed and the entire mountain was no higher than 200 m ASL, the rainbands became even less organized

WANG AND MENG 7 of 18

, 2025, 18, Downloaded from https://agupubs.onlinelibrary.wiley.com/doi/10.1029/2025JD043922 by Peking University Health, Wiley Online Library on [25/09/2025]. See

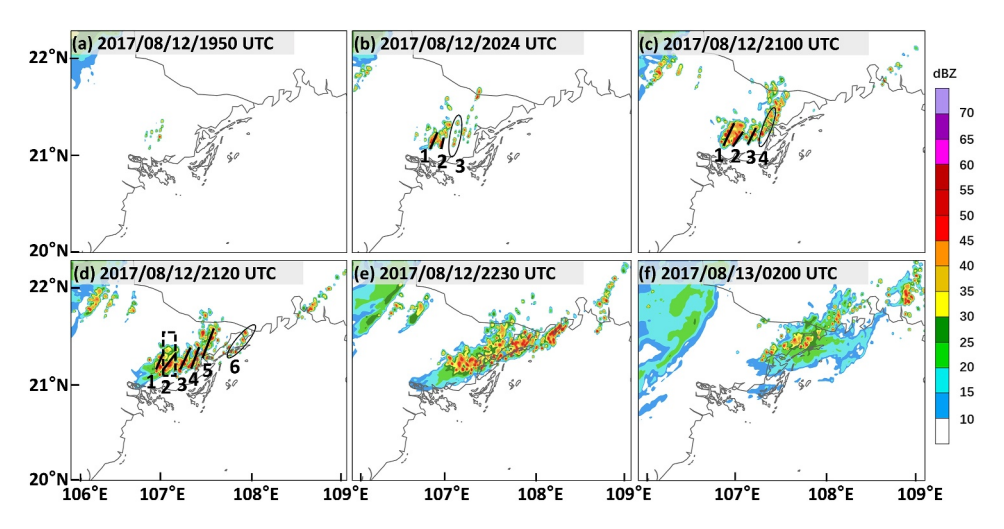


**Figure 6.** Simulated composite radar reflectivity in the CNTL experiment at (a) 1950 UTC, (b) 2024 UTC, (c) 2100 UTC, (d) 2120 UTC, and (e) 2230 UTC on 12 August and (f) 0020 UTC on 13 August. The black lines denote the rainbands of the MPRB system, and the black oval denotes the rainbands to be formed. The black dashed box in (d) denotes the area where the time-latitude section of the zonal maximum reflectivity in rainband 2 was calculated in Figure 10.

with rainbands 2 and 5 completely disappearing, which made the system fail to meet the 20-min threshold of MPRB.

These features of the MPRB were closely related to those of the HCRs. On one hand, with a lower mountain, HCRs became clearer (Figures 12a and 12b). The better organized HCRs in MTs400 and MTs200 were possibly due to stronger boundary layer wind. The mean wind speed in the boundary layer over the narrow mountain region (denoted by the black box in Figure 7a) for MTs400 at 1900 UTC and MTs200 at 1930 UTC, which were 20 min before the formation of their respective HCR, were 7.52 and 7.73 m s<sup>-1</sup>, respectively, which were all conducive to the formation of the HCR ( $U_{\rm CB} > 6$  m s<sup>-1</sup> according to Santellanes et al. (2021)). The slightly stronger mean winds in boundary layer in MTs400 and MTs200 than that in the CNTL (7.09 m s<sup>-1</sup>) were more conducive to HCR formation.

On the other hand, even though MTs400 and MTs200 had a better organized HCR, the height of HCRs became lower and thus might need a longer time to initiate convection. A comparison among the CNTL, MTs400, and MTs200 experiments showed that the HCRs reached the highest altitude in the CNTL experiment and the lowest in the MTs200 experiment (Figures 8a–8c, respectively), which can be clearly seen in terms of the mean top

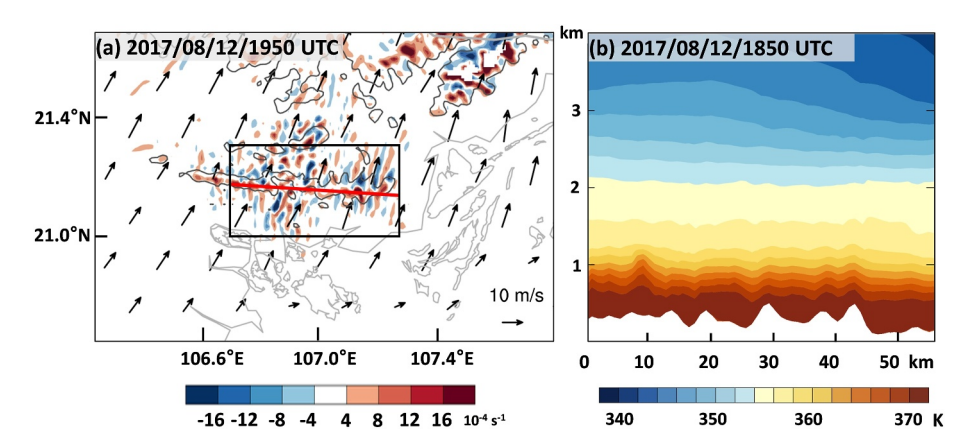


**Figure 7.** (a) Simulated horizontal divergence (shading;  $10^{-4}$  s<sup>-1</sup>) at 1 km ASL and 0–1-km ASL vertical wind shear (black arrow; m s<sup>-1</sup>). The red line in (a) denotes the path for the vertical cross-sections in panel (b) and Figure 8. The black contour denotes a terrain height of 300 m ASL. The gray line denotes the coastal line. The black box was used for calculation for Figures 13 and 17d. (b) The vertical cross-section of the pseudoequivalent potential temperature (shading; K) at 1850 UTC, 20 min before HCR formation, along the red line shown in panel (a).

WANG AND MENG 8 of 18

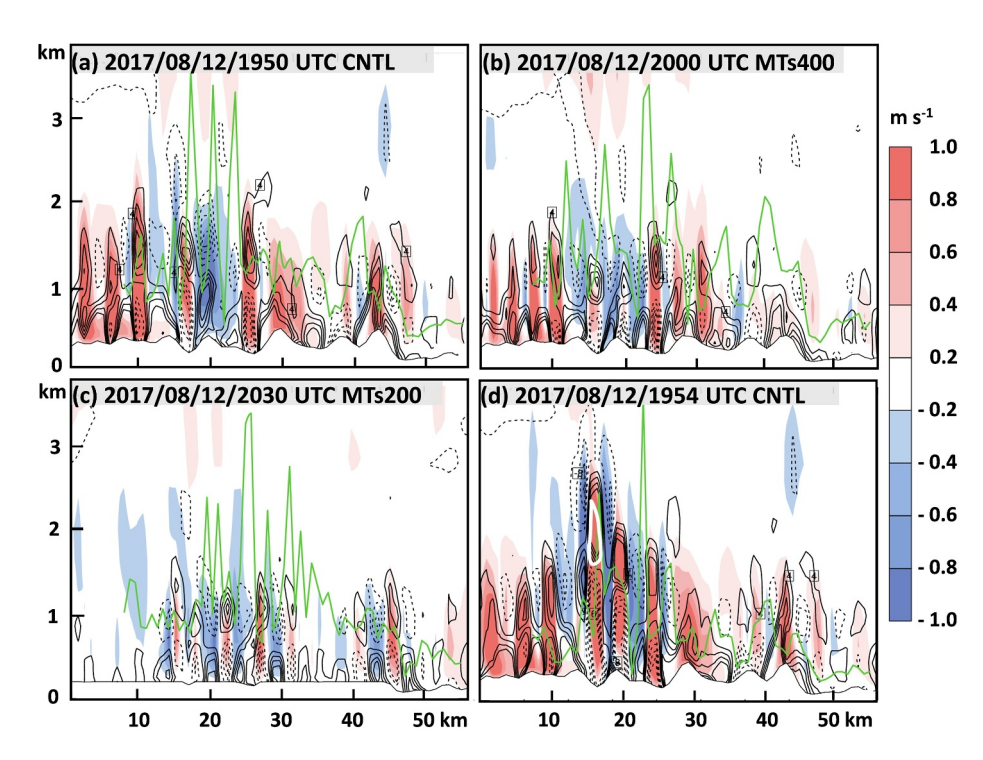


**Figure 8.** Vertical cross-sections (path given in Figure 7a) of vertical velocity (shading;  $s^{-1}$ ), horizontal divergence (contour; solid line for positive value and dashed line for negative value;  $10^{-4}$  s<sup>-1</sup>) in the (a) CNTL, (b) MTs400, and (c) MTs200 experiments at 40 min after the formation of HCRs. The green lines denote the level of free convection (LFC) for the parcel in each column with maximum equivalent potential temperature below 3 km AGL. (d) is the same as (a) but for the time when radar reflectivity of 35 dBZ (white contour) first appeared in the cross-section as a reference for convection initiation.

height of the upward velocity contour of 0.2 m s<sup>-1</sup> that was higher than 1 km ASL in the cross-sections of Figures 8a–8c, with 1.93, 1.71, and 1.36 km ASL for CNTL, MTs400, and MTs200, respectively. The higher HCRs more easily lifted air parcels and initiated convection at earlier times. Figures 8a and 8d clearly show that higher terrain in CNTL lifted the HCR to a greater height, which in turn initiated convection earlier and at more upward branches, thus forming more rainbands. In contrast, in the MTs200 experiment, the lower terrain resulted in a lower HCR. Consequently, the insufficient lifting associated with the lower terrain made much less upward branches of the HCR initiate convection and thus hindered the formation of MPRB. This can be also clearly seen quantitatively in the evolution of the maximum vertical velocity at 1 km ASL (Figure 13), where HCRs formation times are denoted by triangles and convection initiation by dots. HCR formed the earliest in CNTL associated with the earliest enhancement in the upward motion, followed by MTs400 with its upward motion intensification about 10 min later with slightly weaker intensity. Due to an even lower height in MTs200, the HCR formed 40 min behind the CNTL with a much weaker intensity. A similar sequence was observed in their convection initiation times.

Increasing the mountain height and the distances between peaks and valleys in the MTsAdd experiment hindered MPRB formation, and individual rainband structures were replaced with clusters of convection (Figure 11d). The excessively high terrain and sharp peaks in the MTsAdd experiment entirely disrupted HCRs and thus prohibited MPRB formation. There were only a few very small rolls around the narrow mountain (Figure 12d). HCR did not form in MTsAdd possibly due to wind disruption. We calculated the mean wind in the boundary layer of MTsAdd at 1820 UTC, which was 30 min ahead of the time for CNTL mean boundary layer wind calculation, considering that no HCR formed in MTsAdd and the convection initiated 30 min earlier than CNTL. The result was only 5.44 m s<sup>-1</sup>, which was lower than the 6 m s<sup>-1</sup> threshold of Santellanes et al. (2021), and thus failed to form HCR. We also compared the differences in the 0–1 km vertical wind shear between CNTL and MTsAdd experiments. Results showed that the 0–1 km vertical wind shear in MTsAdd was apparently smaller than CNTL (Figure 14a), which is unfavorable for the formation of HCRs. The smaller 0–1 km vertical wind shear in MTsAdd was owing to the smaller wind speed at 1 km ASL in MTsAdd (Figure 14b), possibly due to its higher terrain and vertical distances between valleys and peaks.

WANG AND MENG 9 of 18

nlinelibrary.wiley.com/doi/10.1029/2025JD043922 by Peking University Health, Wiley Online Library on [25/09/2025]. See the Terms and Con

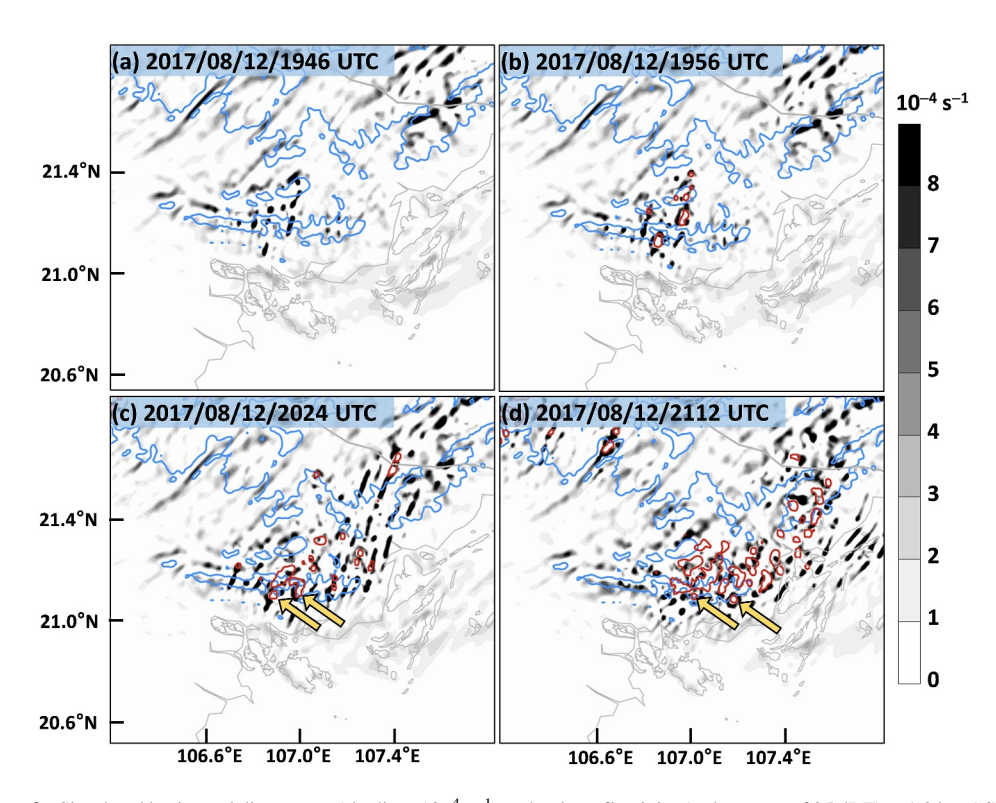


**Figure 9.** Simulated horizontal divergence (shading;  $10^{-4}$  s<sup>-1</sup>) and radar reflectivity (red contour of 35 dBZ) at 1.8 km ASL at (a) 1946 UTC, (b) 1956 UTC, (c) 2024 UTC, and (d) 2112 UTC on 12 August 2017. The yellow arrows denote the position of the cells formed by backbuilding. The blue contour denotes a terrain height of 300 m ASL. The gray line denotes the coastal line

Further experiments suggest that the location of the MPRB system was determined mainly by the narrow mountain, whereas Shiwan Mountain influenced mainly the intensity of the MPRB. In the MTsSmall experiment, in which the narrow mountain was removed, the MPRB system moved northward to near Shiwan Mountain (Figure 11e). HCRs still occurred near the location of the narrow mountain but shifted slightly to the north (Figure 12e). No convection was initiated at the narrow mountain. Instead, convection was initiated in the Shiwan Mountain area (Figure 11e), where HCRs were elevated by this mountain. In the MTsBig experiment, in which

Shiwan Mountain was removed, the MCS still exhibited an MPRB structure at a similar location but was much weaker (Figure 11f).

The above analyses suggest that the formation of MPRB was essentially driven by HCRs elevated by the narrow mountain from 200 m in valleys to 600 m at peaks. Without the occurrence of HCRs, either convection was not initiated at all or convection was no longer organized into a distinct MPRB structure. The excessively high or low mountains either entirely disrupted HCRs or made the HCRs inadequately high.

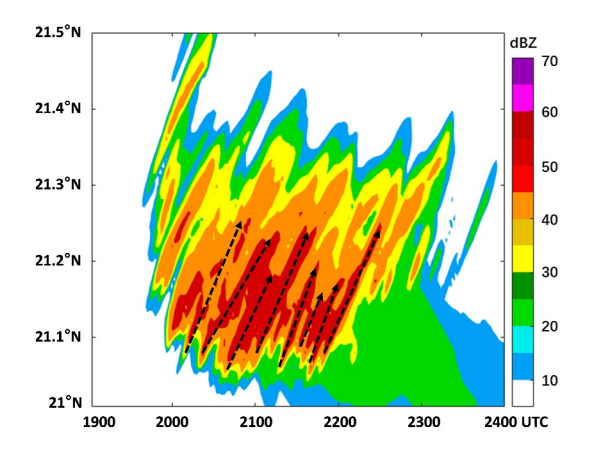


**Figure 10.** Time-latitude section of the zonal maximum reflectivity in a narrow zone containing rainband 2 indicated by the black dashed box in Figure 6d. The slope of the dashed arrow indicates the speed of the cells.

### 4.2.2. Impact of Moisture on HCR Formation

Generally speaking, HCRs tend to appear over flat area. However, HCRs and MPRB all disappeared in the MTs20 experiment (Figures 11c and 12c), in which the whole mountain was removed. Even though the MTs20 had a mean boundary layer wind of  $7.83~{\rm m~s^{-1}}$  at 2110 UTC (20 min before the time when its divergence roll was the longest), also over the box denoted in Figure 7a, which met the 6 m s<sup>-1</sup> threshold of Santellanes et al. (2021), HCR did not form due to a lack of moisture without mountain blocking. Trier et al. (2010) reported that the relative humidity affects the emergence of HCRs.

WANG AND MENG 10 of 18

com/doi/10.1029/2025JD043922 by Peking University Health, Wiley Online Library on [25/09/2025]. See the Terms and Conditions

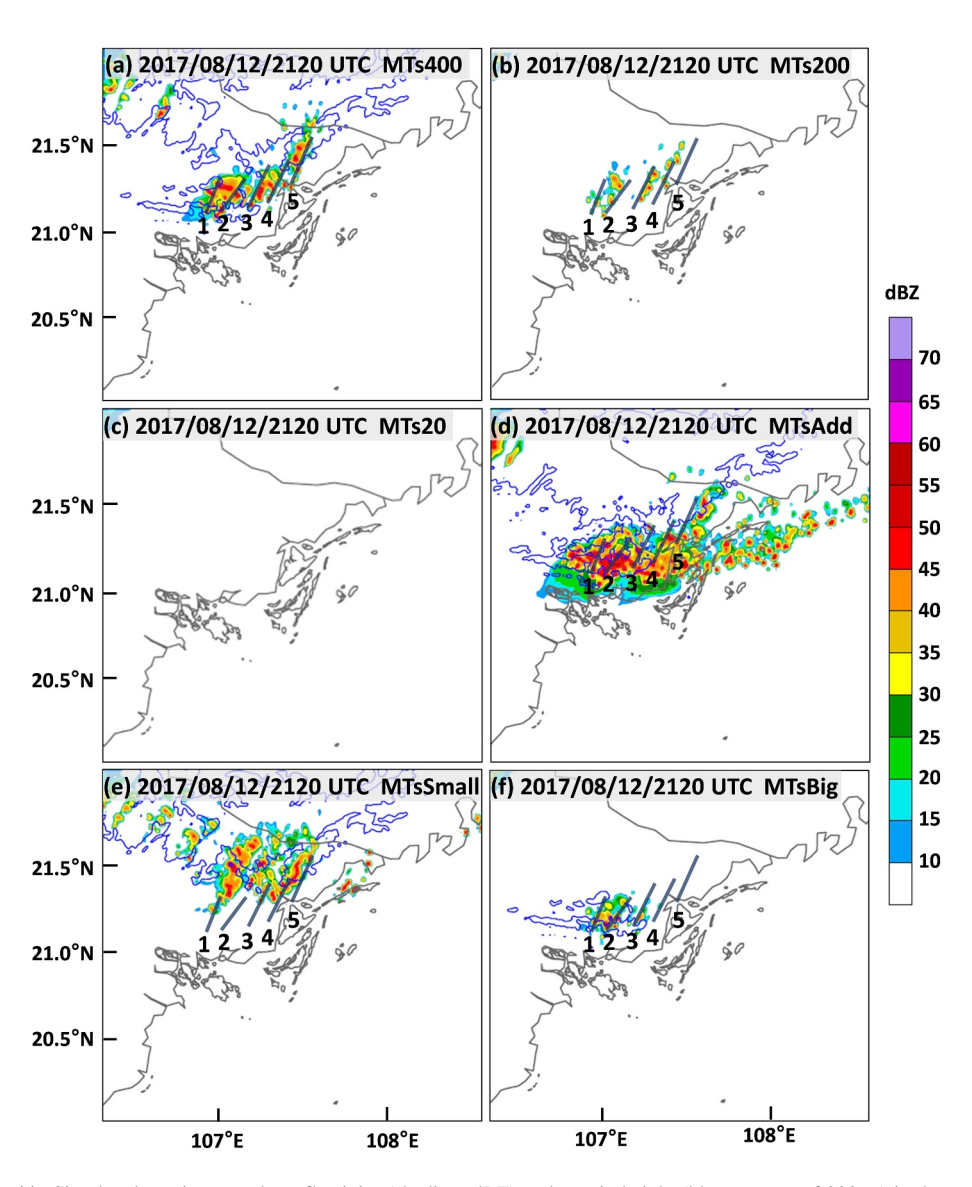


**Figure 11.** Simulated maximum radar reflectivity (shading; dBZ) and terrain height (blue contour of 300 m) in the (a) MTs400, (b) MTs200, (c) MTs20, (d) MTsAdd, (e) MTsSmall, and (f) MTsBig experiments at 2120 UTC on 12 August 2017. The heavy solid blue lines denote the positions of the rainbands in the CNTL experiment at the same time. The gray line denotes the coastal line.

In the CNTL experiment, the relative humidity in the narrow mountain area increased over time because moisture was transported from the sea by southerly winds (Figures 15a and 15b). A comparison of the relative humidity among the different experiments 20 min before the HCRs formed (Figures 15b, 15e, and 15f) indicated that the CNTL, MTs400, and MTs200 experiments encompassed similar relative humidity in the key area, exceeding 90%. However, a comparison between the CNTL and MTs200 experiments both at 1850 UTC revealed that as the mountain height decreased, the relative humidity in the key area also decreased (Figures 15b and 15c, respectively). This was likely due to the flow of water vapor being less obstructed by the lower narrow mountain under the prevailing southwesterly winds. This result suggested that HCRs may not form with insufficient relative humidity. This also explained why, as the mountain height decreased, HCRs formed at a later time, as shown in Figures 12a, 12b and 13.

In the MTs20 experiment (Figure 15d), in which the mountains were almost completely removed, the relative humidity never exceeded 80% throughout the entire period. As a result, water vapor could not accumulate in the coastal areas, leading to the absence of HCRs. In the MTsSmall experiment, in which the narrow mountain was

WANG AND MENG 11 of 18

, 2025, 18, Downloaded from https://agupubs.onlinelibrary.wiley.com/doi/10.1029/2025JD043922 by Peking University Health, Wiley Online Library on [25/09/2025]. See the Terms and Conditions

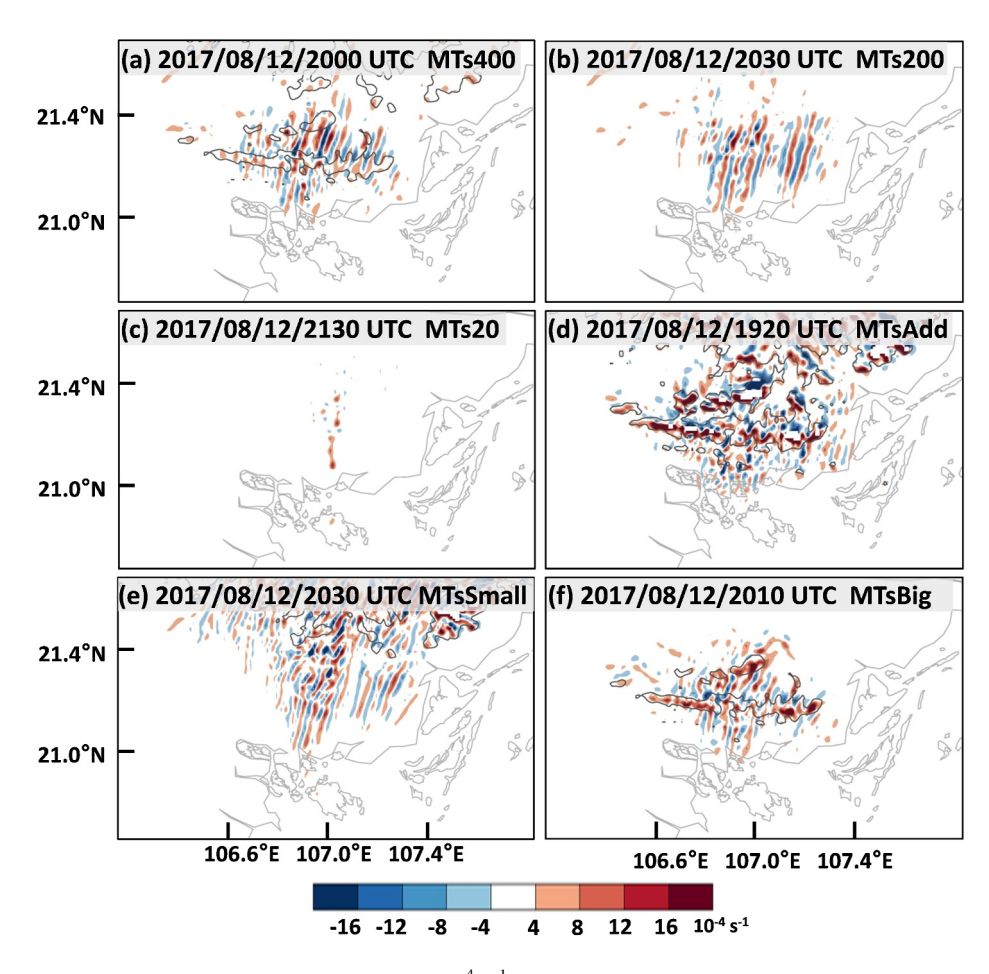


**Figure 12.** Simulated horizontal divergence (shading;  $10^{-4}$  s<sup>-1</sup>) at 1 km ASL and terrain height (black contour of 300 m) in (a) the MTs400 experiment at 2000 UTC, (b) MTs200 at 2030 UTC, (c) MTs20 at 2130 UTC, (d) MTsAdd at 1920 UTC, (e) MTsSmall at 2030 UTC, and (f) MTsBig at 2010 UTC on 12 August 2017. The time was 40 min after the formation of respective HCRs for all experiments except for MTs20, which used the time when the divergence roll was the longest. The gray line denotes the coastal line.

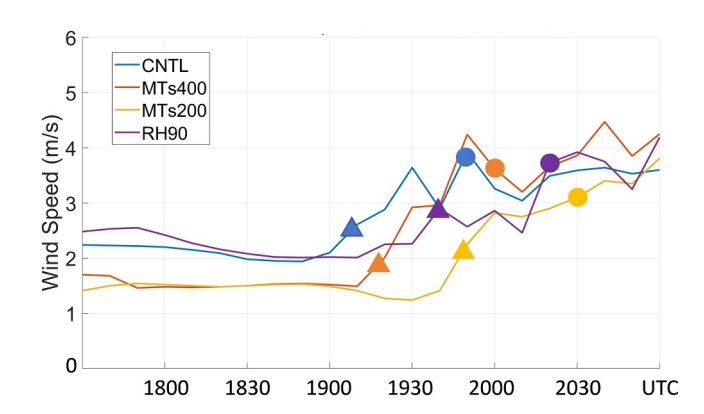


**Figure 13.** Evolution of the maximum vertical velocity at 1 km ASL for CNTL, MTs400, MTs200, and RH90 in the box denoted in Figure 7a. The triangle denotes the time of HCR formation. The dot denotes the time of convection initiation.

removed, water vapor was transported all the way northward and blocked by Shiwan Mountain (Figure 15g). The relative humidity along the coast increased at a much lower speed than that in other experiments. Because high relative humidity was located more to the north, HCRs formed more to the north than those in other experiments did (Figures 12e and 15g). This result suggests that an excessively low relative humidity may prevent the formation of HCRs.

In the MTsBig experiment, in which only Shiwan Mountain was removed, water vapor was still concentrated near the coast. This resulted in a more stable environment in the northern and northeastern parts of the narrow mountain than that in other experiments (Figure 15h). Thus, convection in the MTsBig experiment was initiated only north of the eastern half of the narrow mountain (Figure 11f). The east–west width of the HCRs in the MTsBig experiment was also shorter than that in the other experiments (Figure 12f).

To further confirm the importance of water vapor in the formation of HCRs, we performed an additional RH90 experiment, in which the relative humidity below 2 km ASL was reduced to 90% of the original values in the CNTL experiment. In the RH90 experiment, the magnitude of the relative humidity

WANG AND MENG 12 of 18



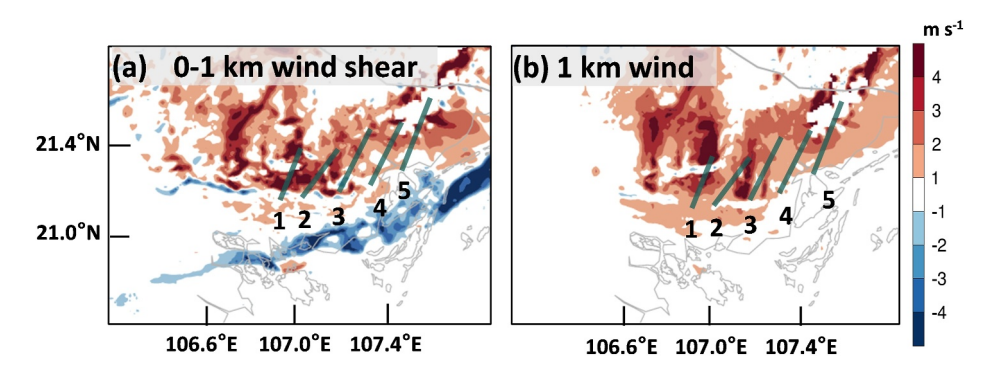


**Figure 14.** The difference between CNTL and MTsAdd experiments of (a) 0–1 km ASL wind shear (shading; m s<sup>-1</sup>) and (b) 1 km ASL wind (shading; m s<sup>-1</sup>). The solid blue lines denote the positions of the rainbands in the CNTL experiment at 2120 UTC on 12 August 2017. Positive value indicates that the value of CNTL is greater than the value of MTsAdd.

at 1850 UTC in the CNTL experiment was reached 30 min later at 1920 UTC (Figure 16a). Correspondingly, HCRs formed 30 min later than those in the CNTL experiment did (at 2020 UTC), and the area of the HCRs decreased (Figure 16b). The time delay in the increase in relative humidity was nearly identical to the time delay in the formation of HCRs, which further verified the close relationship between the relative humidity and HCR formation. Interestingly, a reduction in relative humidity without changing the terrain only delayed the HCR formation and convection initiation by about 30 min relative to the CNTL, while the intensity at the eventual HCR formation and convection initiation were quite similar to the CNTL (Figure 13).

We further examined the moisture convergence in CNTL, MTs20, and RH90 (Figures 17a–17c) to quantitatively analyze the role of water vapor. The results indicated a clear moisture convergence in front of the narrow mountain in the CNTL experiment, which was absent in MTs20, suggesting that the terrain indeed exerted a substantial blocking effect on water vapor. As expected, the moisture convergence in CNTL was slightly larger than in RH90, which also led to the later occurrence of higher relative humidity in the RH90 experiment. The differences in moisture can be clearly seen quantitatively in the temporal variations of specific humidity at 1 km ASL averaged over the narrow mountain region before the formation of HCRs for various experiments (Figure 17d). The dots denote HCR formation times, whose similar values suggested that the water vapor may need to reach certain magnitude for HCR to form. The MTs20 stayed too low, and thus failed in forming HCR. The sensitivity of HCRs formation to moisture further confirmed the important role of convective instability for the HCR formation in this case.

### 5. Conclusions

In this study, the formation mechanism of an initiation-type MPRB event that occurred on 12 August 2017, in the western coastal area of the Beibu Gulf, was investigated via high-resolution numerical simulations with the WRF model v4.4 and terrain modification experiments. Our previous work revealed that initiation-type MPRBs in China exhibit the highest frequency in mountainous areas along the western coast of the Beibu Gulf, where there is an east–west-oriented low mountain with frequent HCRs.

Based on observations and simulations, this study revealed that the MPRB system resulted from the backbuilding process of convection over the updraft branches of HCRs elevated by low mountains from 200 m in valleys to 600 m at peaks. HCRs started to form with clear alternating positive and negative divergence lines 40 min before convection initiation, aligning with the direction of the 0–1 km vertical wind shear with a height of approximately 1–2 km ASL, with an aspect ratio of 6.2 in a mean boundary layer wind of 7.09 m s<sup>-1</sup>, mainly attributed to convective instability. The area where the MPRB system formed exhibited apparent unstable stratification at lower levels and vertical wind shear as well as rich moisture.

A mechanism for the formation of an MPRB through HCR-mountain coupling was proposed (Figure 18). With the low-level jet transporting rich moisture toward a low mountain orienting perpendicular to the wind direction, moisture is pooled in front of the mountain, enhancing convective instability and forming HCR. Convective initiation occurs over the higher updraft branches of the HCR elevated by the mountain. With new cells being continuously initiated upstream of the mountain area through a backbuilding process, parallel convective

WANG AND MENG 13 of 18

21698996, 2025, 18, Downloaded from https://agupubs.onlinelibrary.wiley.com/doi/10.1029/2025/D043922 by Peking University Health, Wiley Online Library on [25/09/2025]. See the Terms and Conditions (https://onlinelibrary.wiley.com/ems-and-conditions) on Wiley Online Library for rules of use; OA articles are governed by the applicable Creve

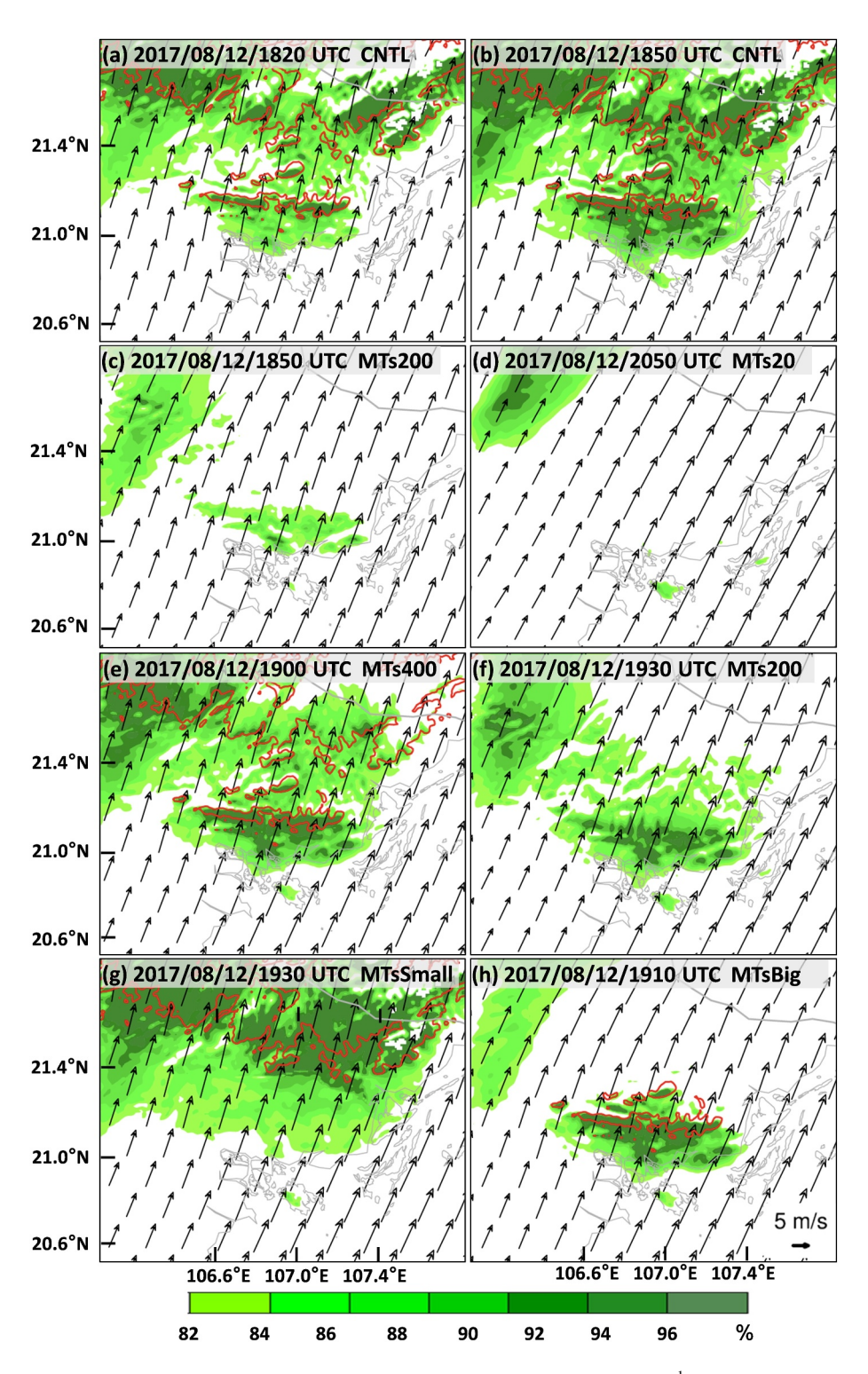


**Figure 15.** Relative humidity (shading; %) at 1 km ASL; 1-km wind vector (black arrow; m s $^{-1}$ ) in the CNTL experiment at (a) 1820 UTC, (b) 1850 UTC, (c) MTs200 at 1850 UTC, (d) MTs20 at 2050 UTC, (e) MTs400 at 1900 UTC, (f) MTs200 at 1930 UTC, (g) MTsSmall at 1930 UTC, and (h) MTsBig at 1910 UTC. The red contour denotes a terrain height of 300 m ASL. The gray lines denote coastal lines.

WANG AND MENG 14 of 18

21698996, 2025, 18, Downloaded from https://agupubs.onlinelibrary.wiley.com/doi/10.1029/2025JD043922 by Peking University Health, Wiley Online (10.1029/2025JD043922) and the control of t

**Figure 16.** (a) Relative humidity (shading; %) at 1 km ASL and 1-km wind vector (black arrow; m s<sup>-1</sup>) in the RH90 experiment at 1920 UTC on 12 August 2017 and (b) simulated horizontal divergence (shading;  $10^{-4}$  s<sup>-1</sup>) in the RH90 experiment at 2020 UTC on 12 August 2017. The terrain height of 300 m ASL is denoted by red and black contours in (a) and (b), respectively.

rainbands develop to form the MPRB. If the mountain is not high enough to lift the air parcel surpass level of free convection, convective initiation may not occur even if HCR indeed occurs.

The results revealed that no MPRB was generated without the formation of HCRs and that the pure lifting of HCRs could not produce MPRB either. Although high mountains may slightly disrupt HCR structures, destructive impacts were not observed for mountains from 200 m in valleys to 600 m at peaks in this region. With HCRs elevated by such low mountains, convection initiation occurred more easily above the updraft branches of the HCRs. As the mountain height decreased, even though the HCRs became better organized, the MPRB structure weakened or even disappeared due to the lower lifting of HCRs. However, if the mountain became excessively high, as in the MTsAdd experiment in which the terrain height was increased to 400–1,200 m ASL, HCRs were completely eliminated by the terrain, and no MPRB formed.

Coastal low mountains, as well as the northern Shiwan Mountain, affected the structure of HCRs by influencing the distribution of water vapor. Coastal mountains were beneficial for HCR formation because the flow of

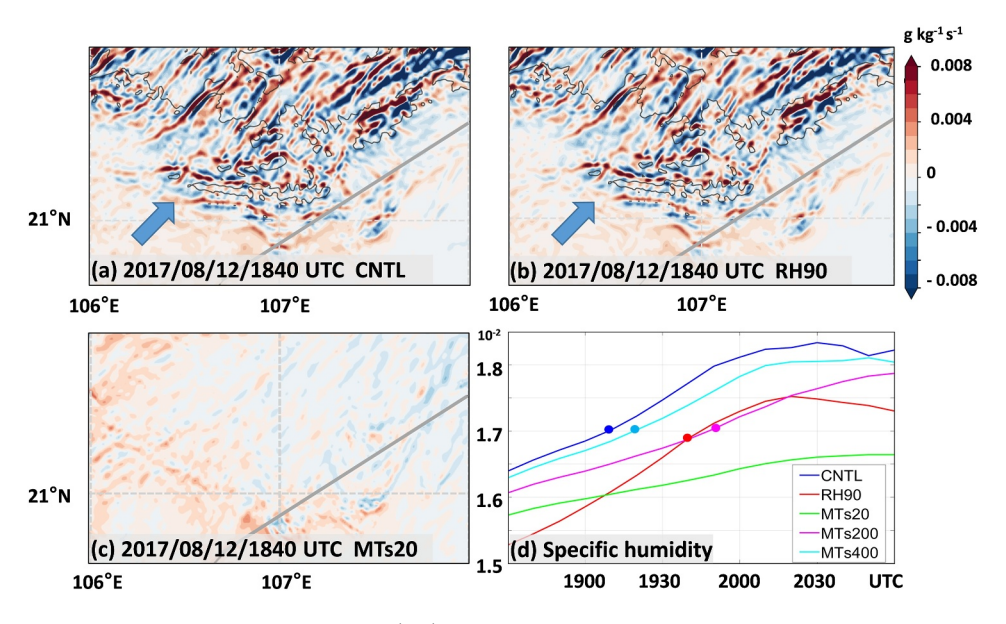


**Figure 17.** Moisture convergence (shading; g  $kg^{-1}$  s<sup>-1</sup>) at 1 km ASL in (a) CNTL, (b) RH90, and (c) MTs20 experiments at 1840 UTC on 12 August 2017. The terrain height at 300 m ASL is denoted by black contours. The gray line denotes coarse-resolution coastline. The blue arrow denotes area with significant differences in moisture convergence. (d) Time evolution of specific humidity at 1 km ASL averaged over the black box in Figure 7a. The dots represent the HCR formation times of different experiments.

WANG AND MENG 15 of 18

com/doi/10.1029/2025JD043922 by Peking University Health, Wiley Online Library on [25/09/2025]. See the Term

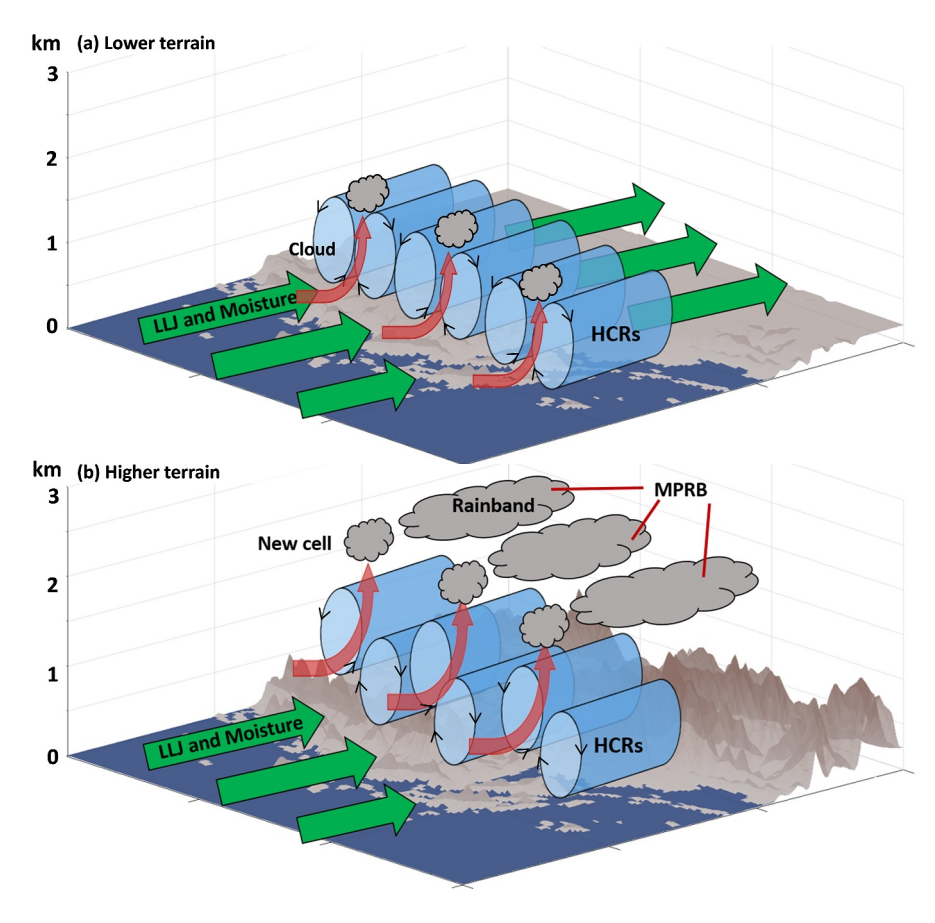


Figure 18. Schematic of the impacts of coastal terrain on HCRs producing an MPRB.

sufficient water vapor from the southern sea was blocked, and water vapor accumulated in this region. Reducing relative humidity by 10% of its original value substantially delayed the formation of HCRs. Similarly, reducing the height of the mountains yielded the same effect. The removal of the narrow mountain near the coast caused the area of high water vapor and HCRs to shift northward. After totally removing both the Shiwan Mountain and the narrow mountain as in MTs20, moisture got too low to form HCRS without terrain blocking.

This study reveals a novel mechanism where HCRs couple with coastal low mountains to trigger and organize convection into an MPRB MCS, which completes previous studies that mainly emphasized cold pool outflows. Such findings also extend current knowledge on the role of HCRs in convection initiation by demonstrating that low mountains can directly influence boundary layer roll structures to initiate organized rainfall without additional boundaries. This mechanism likely operates in other coastal regions with similar topography and environmental conditions, suggesting that integrating terrain-HCR coupling into forecasting frameworks could improve predictions of MPRB-related heavy rainfall and associated flooding hazards in vulnerable coastal zones.

### **Data Availability Statement**

Radar data were provided by the National Meteorological Information Center of the China Meteorological Administration (https://data.cma.cn/data/cdcindex/cid/0b9164954813c573.html). The ERA5 hourly data from 2007 to 2021 on pressure levels and single levels are available respectively at Hersbach et al. (2023a, 2023b). The FNL data (National Centers for Environmental Prediction/National Weather Service/NOAA/U.S. Department of Commerce 2000) are obtained from https://rda.ucar.edu/datasets/d083002/.

WANG AND MENG 16 of 18

#### Acknowledgments

This work was sponsored by the National Natural Science Foundation of China (Grants 42030604 and 41875051).

### References

- American Meteorological Society. (2024). Horizontal convective rolls. Glossary of Meteorology. Retrieved from http://glossary.ametsoc.org/wiki/Horizontalconvectiverolls
- Bai, L., Chen, G., & Huang, L. (2020). Image processing of radar mosaics for the climatology of convection initiation in south China. *Journal of Applied Meteorology and Climatology*, 59(1), 65–81. https://doi.org/10.1175/JAMC-D-19-0081.1
- Banghoff, J. R., Sorberm, J. D., Stensrud, D. J., Young, G. S., & Kumjian, M. R. (2020). A 10-year warm-season climatology of horizontal convective rolls and cellular convection in central Oklahoma. *Monthly Weather Review*, 148(1), 21–42. https://doi.org/10.1175/MWR-D-19-0136.1
- Collins, W. D., Rasch, P. J., Boville, B. A., Hack, J. J., McCaa, J. R., Williamson, D. L., et al. (2004). Description of the NCAR Community Atmosphere Model (CAM 3.0). NCAR Tech. Note NCAR/TN-4641STR, 214. https://doi.org/10.5065/D63N21CH
- Doswell, C. A., Brooks, H. E., & Maddox, R. A. (1996). Flash flood forecasting: An ingredients-based methodology. *Weather and Forecasting*, 11(4), 560–581. https://doi.org/10.1175/1520-0434(1996)011<0560:FFFAIB>2.0.CO;2
- Du, Y., & Chen, G. (2019). Heavy rainfalls associated with double low-level jets over Southern China. Part II: Convection initiation. *Monthly Weather Review*, 147(2), 543–565. https://doi.org/10.1175/MWR-D-18-0102.1
- Weather Review, 14/(2), 543–565. https://doi.org/10.11/5/MWR-D-18-0102.1

  Du, Y., Shen, Y., & Chen, G. (2022). Influence of coastal marine boundary layer jets on rainfall in South China. Advances in Atmospheric
- Sciences, 39(5), 782–801. https://doi.org/10.1007/s00376-021-1195-7

  Duhdia, J. (1996). A multi-layer soil temperature model for MM5. In *Preprints, the sixth PSU/NCAR mesoscale model users' workshop*, 22–24

  July 1996. (pp. 49–50).
- Etling, D., & Brown, R. (1993). Roll vortices in the planetary boundary layer: A review. Boundary-Layer Meteorology, 65(3), 215–248. https://doi.org/10.1007/BF00705527
- Gol.org/10.1007/BF00705527

  Fovell, R. G. (2005). Convective initiation ahead of the sea-breeze front. *Monthly Weather Review*, 133(1), 264–278. https://doi.org/10.1175/
- Fulton, R. A., Breidenbach, J. P., Seo, D., Miller, D. A., & O'Bannon, T. (1998). The WSR-88D rainfall algorithm. Weather and Forecasting, 13,
- 377–395. https://doi.org/10.1175/1520-0434(1998)013,0377:TWRA.2.0.CO;2
  Gallus, W. A., Snook, N. A., & Johnson, E. V. (2008). Spring and summer severe weather reports over the midwest as a function of convective
- mode: A preliminary study. Weather and Forecasting, 23(1), 101–113. https://doi.org/10.1175/2007WAF2006120.1
- Grell, G. A., & Freitas, S. R. (2014). A scale and aerosol aware stochastic convective parameterization for weather and air quality modeling. Atmospheric Chemistry and Physics, 14(10), 5233–5250. https://doi.org/10.5194/acp-14-5233-2014
- Hersbach, H., Bell, B., Berrisford, P., Biavati, G., Horányi, A., Muñoz Sabater, J., et al. (2023a). ERA5 hourly data on pressure levels from 1940 to present [Dataset]. Copernicus Climate Change Service (C3S) Climate Data Store (CDS). https://doi.org/10.24381/cds.bd0915c6
- Hersbach, H., Bell, B., Berrisford, P., Biavati, G., Horányi, A., Muñoz Sabater, J., et al. (2023b). ERA5 hourly data on single levels from 1940 to present [Dataset]. Copernicus Climate Change Service (C3S) Climate Data Store (CDS). https://doi.org/10.24381/cds.adbb2d47
- Hong, S.-Y., Noh, Y., & Dudhia, J. (2006). A new vertical diffusion package with an explicit treatment of entrainment processes. *Monthly Weather Review*, 134(9), 2318–2341. https://doi.org/10.1175/MWR3199.1
- Jimenez, P. A., Dudhia, J., Gonzalez-Rouco, J. F., Navarro, J., Montavez, J. P., & Garcia–Bustamante, E. (2012). A revised scheme for the WRF surface layer formulation. Monthly Weather Review, 140(3), 898–918. https://doi.org/10.1175/MWR-D-11-00056.1
- Kong, H., Zhang, Q. H., Du, Y., & Zhang, F. (2020). Characteristics of coastal low-level jets over Beibu Gulf, China, during the early warm season. *Journal of Geophysical Research: Atmospheres*, 125(14), e2019JD031918. https://doi.org/10.1029/2019JD031918
- Li, S., Meng, Z., & Wu, N. (2021). A preliminary study on the organizational modes of mesoscale convective systems associated with warm-sector heavy rainfall in South China. *Journal of Geophysical Research: Atmospheres*, 126(16), e2021JD034587. https://doi.org/10.1029/2021JD034587
- Liu, X., Luo, Y., Guan, Z., & Zhang, D.-L. (2018). An extreme rainfall event in coastal South China during SCMREX-2014: Formation and roles of rainband and echo trainings. *Journal of Geophysical Research: Atmospheres*, 123(17), 9256–9278. https://doi.org/10.1029/2018JD028418
- Luo, Y., Gong, Y., & Zhang, D.-L. (2014). Initiation and organizational modes of an extreme-rain-producing mesoscale convective system along a Mei-Yu front in East China. *Monthly Weather Review*, 142(1), 203–221. https://doi.org/10.1175/MWR-D-13-00111.1
- Morrison, H., Thompson, G., & Tatarskii, V. (2009). Impact of cloud microphysics on the development of trailing stratiform precipitation in a simulated squall line: Comparison of one- and two-moment schemes. *Monthly Weather Review*, 137(3), 991–1007. https://doi.org/10.1175/2008MWR2556.1
- Parker, M. D., & Johnson, R. H. (2000). Organizational modes of midlatitude mesoscale convective systems. *Monthly Weather Review*, 128(10), 3413–3436. https://doi.org/10.1175/1520-0493(2001)129<3413:OMOMMC>2.0.CO;2
- Santellanes, S. R., Young, G. S., Stensrud, D. J., Kumjian, M. R., & Pan, Y. (2021). Environmental conditions associated with horizontal convective rolls, cellular convection, and no organized circulations. *Monthly Weather Review*, 149(5), 1305–1316. https://doi.org/10.1175/ MWR-D-20-0207.1
- Su, A., Zheng, Y., & Zhang, N. (2022). A review of research on boundary convergence lines triggering of deep and moist convection. Acta Meteorologica Sinica, 80(2), 177–189.
- Tian, W., Parker, D. J., & Kilburn, C. A. D. (2003). Observations and numerical simulation of atmospheric cellular convection over mesoscale topography. *Monthly Weather Review*, 131(1), 222–235. https://doi.org/10.1175/1520-0493(2003)131<0222:oansoa>2.0.co:2
- Trier, S. B., Sharman, R. D., Fovell, R. G., & Frehlich, R. G. (2010). Numerical simulation of radial cloud bands within the upper-level outflow of an observed mesoscale convective system. *Journal of the Atmospheric Sciences*, 67(9), 2990–2999. https://doi.org/10.1175/2010jas3531.1
- Wang, H., Luo, Y., & Jou, B. (2014). Initiation, maintenance, and properties of convection in an extreme rainfall event during SCMREX: Observational analysis. *Journal of Geophysical Research: Atmospheres*, 119(23), 13206–13232. https://doi.org/10.1002/2014JD022339
- Wang, P., & Meng, Z. (2023). General features of MCSs with the organization of multiple parallel rain bands in China. *Monthly Weather Review*, 151(9), 2485–2499. https://doi.org/10.1175/MWR-D-22-0304.1
- Wang, Q., Zhang, Y., Zhu, K., Tan, Z., & Xue, M. (2021). A case study of the initiation of parallel convective lines back-building from the south side of a Mei-Yu front over complex terrain. Advances in Atmospheric Sciences, 38(5), 717–736. https://doi.org/10.1007/s00376-020-0216-2
- Stue, M., & Martin, W. J. (2006). A high-resolution modeling study of the 24 May 2002 dryline case during IHOP. Part I: Numerical simulation and general evolution of the dryline and convection. *Monthly Weather Review*, 134(1), 149–171. https://doi.org/10.1175/MWR.3071.1
- Young, G. S., Kristovich, D. A., Hjelmfelt, M. R., & Foster, R. C. (2002). Supplement to rolls, streets, waves, and more. Bulletin of the American Meteorological Society, 83(7), 1001. https://doi.org/10.1175/BAMS-83-7-Young

WANG AND MENG 17 of 18



### Journal of Geophysical Research: Atmospheres

- 10.1029/2025JD043922
- Zhang, M., & Meng, Z. (2019). Warm-sector heavy rainfall in southern China and its WRF simulation evaluation: A low-level-jet perspective. Monthly Weather Review, 147(12), 4461–4480. https://doi.org/10.1175/mwr-d-19-0110.1
- Zheng, L., Sun, J., Zhang, X., & Liu, C. (2013). Organizational modes of mesoscale convective systems. Weather and Forecasting, 28(5), 1081–1098. https://doi.org/10.1175/WAF-D-12-00088.1
- Zhu, L., Bai, L., Chen, G., Sun, Y. Q., & Meng, Z. (2021). Convection initiation associated with ambient winds and local circulations over a tropical island in South China. *Geophysical Research Letters*, 48(16), e2021GL094382. https://doi.org/10.1029/2021GL094382
- Zhu, P., Wang, Y., Chen, S. S., Curcic, M., & Gao, C. (2015). Impact of storm-induced cooling of sea surface temperature on large turbulent eddies and vertical turbulent transport in the atmospheric boundary layer of Hurricane ISAAC. *Journal of Geophysical Research: Oceans*, 121(1), 861–876. https://doi.org/10.1002/2015JC011320

WANG AND MENG 18 of 18